X-band two-stage rf pulse compression system with correction cavity chain

Xiancai Lin, Hao Zha, Jiaru Shi,* Yuliang Jiang, Fangjun Hu, Weihang Gu, Qiang Gao, and Huaibi Chen

Department of Engineering Physics, Tsinghua University, Beijing CN-100084, China and Key Laboratory of Particle and Radiation Imaging, Ministry of Education, Tsinghua University, Beijing CN-100084, China

(Received 19 September 2022; accepted 28 November 2022; published 13 December 2022)

A compact *X*-band two-stage rf pulse compression system has been successfully designed, fabricated, and tested at Tsinghua *X*-band high-power test stand. The pulse compression system consists of a correction cavity chain, a first-stage, and a second-stage storage cavity. The correction cavity chain adopts a new design whose transmission loss and length are reduced by half compared with the old one. A detuning device is applied to the second-stage storage cavity so that the system can work in one-stage or alternatively two-stage compression mode. In the one-stage compression mode, a 150-ns, 70-MW flattop output, with a standard deviation of 1.5% in amplitude and 1° in phase, was generated with a gain factor of 3. In the two-stage compression mode, a first two-stage pulse compression experiment with correction cavities in the *X* band was performed. A peak power of 320 MW was achieved with a gain factor of 9.7 and full-width at half-maximum pulse durations of 53 ns.

DOI: 10.1103/PhysRevAccelBeams.25.120401

I. INTRODUCTION

In the particle accelerator field, the rf pulse compressor is a component that can compress a long input rf pulse to a short one with a higher amplitude and enhance the beam energy gain of an accelerating structure. The first and most commonly used rf pulse compressor in particle accelerators is SLAC Energy Doubler (SLED) [1]. SLED is a passive component triggered by the phase reversal and has very stable performance in a klystron-based microwave system. In recent decades, SLED has been playing an essential role in various accelerator facilities, such as the Large Electron-Positron Collider (LEP) at CERN [2], LINAC Coherent Light Source (LCLS) at SLAC [3,4], KEK B Factory (KEKB) [5,6], Pohang Accelerator Laboratory X-ray Free Electron Laser (PAL-XFEL) [7], and Shanghai Soft X-ray Free-Electron Laser facility (SXFEL) at SINAP [8,9].

Over the past 50 years, rf pulse compressors with resonant cavities have been developed. A barrel open cavity (BOC) was invented to realize a very high intrinsic quality factor [10,11]. It uses a whispering gallery mode operating in a resonant rotating wave regime, where a single cavity is sufficient for pulse compression. In 2014, a very compact pulse compressor utilizing a spherical cavity and a dual-mode polarizer was invented [12,13], which has been applied in the *X* band [14], the C band [15], and the S band [16]. Besides the spherical cavity, other high Q cavities working with the dual-mode polarizer have also been developed, including the corrugated cylindrical cavity [17] and bowl-shaped cavity [18].

The aforementioned rf pulse compressors generate exponentially decaying pulses owing to the energy-releasing process of a high-Q resonant cavity. However, a flattop output is more favorable because it can accelerate multiple bunches and reduce the maximum transient surface field of the structure. There are three ways to generate flattop output with a pulse compressor. The first one is applying amplitude modulation (AM) to the input pulse [19,20] of a cavity-base pulse compressor. Nevertheless, it will lower the pulse compression efficiency. The second one is using a SLED-II [21,22], which is based on the delay line. Two 29-m *X*-band delay lines to generate 400-ns output have been realized at the NLCTA platform at SLAC [23]. However, the large size of SLED-II makes it hard to fit in a compact platform. The third one is inserting a correction cavity chain (CC) to correct the declining output pulse of the cavity-based pulse compressor, which has a high efficiency close to SLED-II and maintains a very compact size (less than 0.5 m in the *X* band). This method was proposed in 1992 [24] and has been realized in 2019 [25,26]. In this article, we will present a method to improve the design of the CC and reduce its length and transmission loss by half.

The flattop output of the pulse compressor with CC can be compressed once more to generate higher power, which is called two-stage pulse compression. In 2019, Tsinghua University developed an S-band two-stage pulse

*shij@tsinghua.edu.cn

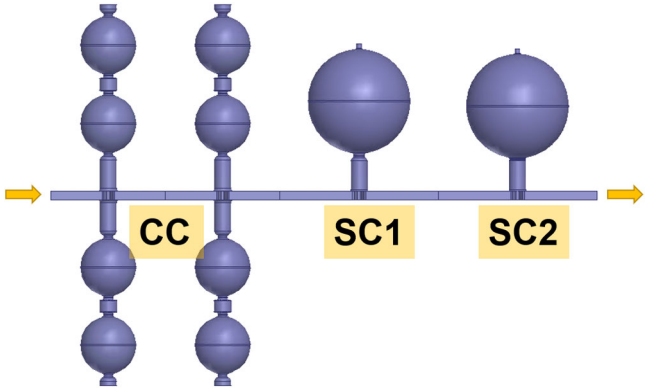

FIG. 1. Vacuum model of the X-band two-stage pulse compression system.

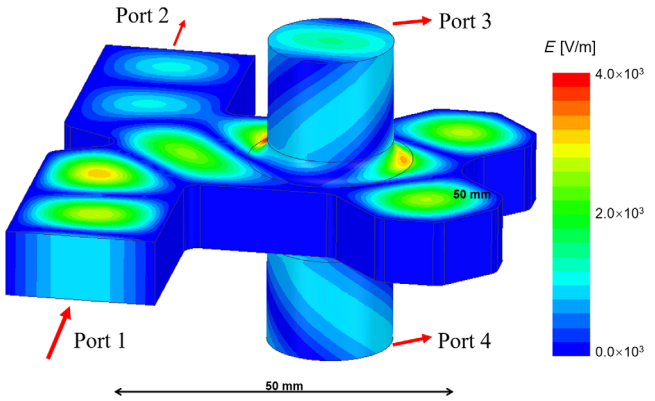

FIG. 2. Geometry of the expanded polarizer and the transient E-field distribution with 1-W input power fed from port 1.

compression system for the first time [27]. In this study, we extended this technique to the X band and developed a new two-stage pulse compression system. The vacuum model of this system is shown in Fig. 1. The pulse compression system consists of a CC, a first-stage storage cavity (SC1), and a second-stage storage cavity (SC2). The system can switch between the one-stage and two-stage pulse compression by detuning the SC2 with a detuning device. The first two-stage pulse compression experiment with CC in the X band is also presented in this paper.

The content of this paper is organized as follows: In Sec. II, we introduce our method to improve the CC design by expanding the dual-mode polarizer. In Sec. III, the parametric optimization and rf design of the system are introduced. In Sec. IV, a tuning strategy is proposed to simplify the tuning of the CC and two storage cavities, and the measurement results after fabrication are shown. High-power tests were performed at Tsinghua X-band high-power test stand (TPOT-X), including two-stage and one-stage pulse compressions, which are presented in detail in Sec. V.

II. EXPANSION OF THE POLARIZER IN A CORRECTION CAVITY CHAIN

As an insertion component to correct the rf pulse shape and improve the compression efficiency, the transmission loss of the CC is a non-negligible factor. The primary transmission loss comes from the polarizers, with an experimental value of 2.5% for each from the former rf measurement [26]. Therefore, reducing the number of polarizers can effectively increase pulse compression efficiency.

The dual-mode polarizer is a three-port rf component with two rectangular waveguide ports and a cylindrical waveguide port. Two orthogonal TE_{11} modes are stimulated at the cylindrical waveguide port when the signal is imported from one of the rectangular waveguide ports. These TE_{11} modes can excite corresponding polarized modes inside the resonant cavity. As a result, the dual-mode polarizer with a resonant cavity has the same function as a 3-dB hybrid with two identical resonant cavities [14].

The dual-mode polarizer has many forms [12,13,25,28,29]. We utilized the H-plane form with a cylindrical waveguide at the bottom of it [13,15,16] in this design for the CC. The end of the bottom waveguide was expanded as an additional cylindrical waveguide port (port 4), as shown in Fig. 2. The transient E-field distribution of the expanded polarizer with power fed from port 1 is also shown. The full S-parameters of this component are shown in Table I. S:i:j in the table corresponds to the jth mode in the ith port while the serial number of ports is listed in Fig. 2.

An expanded polarizer can be attached with two resonant cavities working at different frequencies, which can be applied to the CC. Next, we will prove this feature by cascading its S-parameters with the reflection spectra of two resonant cavities. To simplify the cascade algorithm, we expressed the S-parameters of the polarizer as a block matrix:

$$\begin{bmatrix} \mathbf{b} \\ \mathbf{b_1} \end{bmatrix} = \begin{bmatrix} \mathbf{A} & \mathbf{B} \\ \mathbf{C} & \mathbf{D} \end{bmatrix} \begin{bmatrix} \mathbf{a} \\ \mathbf{a_1} \end{bmatrix}, \tag{1}$$

where $\mathbf{a}$, $\mathbf{b}$ are input and output vectors of free ports, $\mathbf{a}_1$, $\mathbf{b}_1$ are input and output vectors of ports to be cascaded, and

TABLE I. Simulated scattering matrix of the expanded polarizer.

dB (deg)	S:1:1	S:2:1	S:3:1	S:3:2	S:4:1	S:4:2
S:1:1	−41.2 (−82.2)	−8.2 (33.2)	−6.8 (47.2)	−6.7 (−42.5)	−6.8 (−150.0)	−6.7 (120.9)
S:2:1	−8.2 (33.2)	−41.2 (−82.1)	−6.7 (−35.1)	−6.8 (54.9)	−6.7 (161.5)	−6.8 (−108.0)
S:3:1	−6.8 (47.2)	−6.7 (−35.1)	−8.3 (−86.2)	−35.5 (18.7)	−4.1 (−53.1)	−14.5 (122.3)
S:3:2	−6.7 (−42.5)	−6.8 (54.9)	−35.5 (18.7)	−8.2 (−86.9)	−14.4 (−49.6)	−4.1 (−54.2)
S:4:1	−6.8 (−150.0)	−6.7 (161.5)	−4.1 (−53.1)	−14.4 (−49.6)	−8.3 (−85.0)	−38.0 (18.7)
S:4:2	−6.7 (120.9)	−6.8 (−108.0)	−14.5 (122.3)	−4.1 (−54.2)	−38.0 (18.7)	−8.2 (−88.1)

$\mathbf{A}, \mathbf{B}, \mathbf{C}, \mathbf{D}$ are the corresponding block matrix. In this case, ports 1 and 2 are free ports, whereas ports 3 and 4 are cascaded ports. The relationship between input and output vectors of cascaded ports is expressed with a relation matrix $\mathbf{T}$ as

$$\mathbf{a_1} = \mathbf{T}\mathbf{b_1}. \tag{2}$$

Substituting Eq. (2) into Eq. (1) and solving the relationship of input and output vectors of free ports. The scattering matrix after the cascade can be expressed as

$$\mathbf{b} = \mathbf{S}\mathbf{a}, \qquad \mathbf{S} = \mathbf{A} + \mathbf{B}(\mathbf{T^{-1}} - \mathbf{D})^{-1}\mathbf{C}. \tag{3}$$

Ports 3 and 4 will be attached with two different cavities. The relation matrix is expressed as $\mathbf{T} = \mathrm{diag}\{\Gamma_1, \Gamma_1, \Gamma_2, \Gamma_2\}$, where Γ_1 and Γ_2 are reflection spectra of two cavities attached to ports 3 and 4. Γ_1 and Γ_2 are repeated twice because two polarized modes are stimulated in the cavity. The reflection spectrum of a cavity can be obtained from its equivalent circuit model [30]:

$$\Gamma = \frac{(\beta - 1) - jQ_0\xi}{(\beta + 1) + jQ_0\xi}, \tag{4}$$

where β is the coupling factor of the cavity, $\xi = f/f_0 - f_0/f$, f_0 is the resonant frequency, and Q_0 is the intrinsic quality factor. Two cavities are used in this calculation to prove the properties of an expanded polarizer. Frequencies of them are set to 11.414 and 11.434 GHz, respectively. Both of them have a $Q_0 = 50,000$ and $\beta = 2$. The transmission spectrum calculated with Eq. (3) is shown in Fig. 3. A schematic diagram of the expanded polarizer with two cavities is also shown. The transmission spectrum of two cascaded polarizers is also presented for comparison. Two transmission spectra are almost identical, proving that an expanded polarizer has the same function as two normal ones when attached to two cavities at different frequencies.

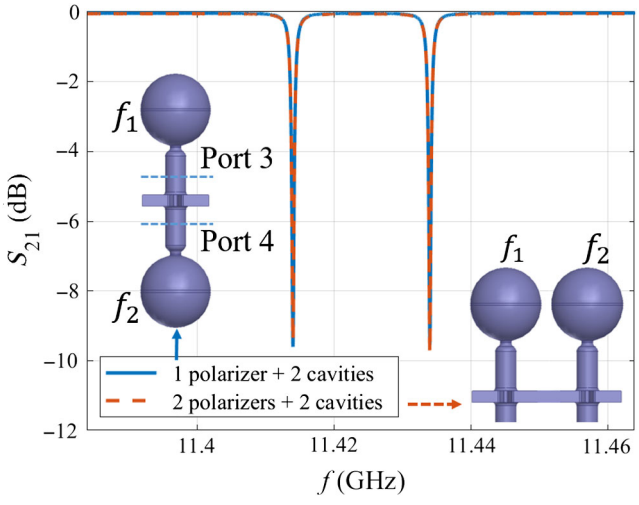

FIG. 3. Transmission spectra of the expanded polarizer with two cavities at different frequencies compared with two cascaded normal polarizers with the same cavities.

The theory of expanding the polarizer is illustrated as follows. When the cavity at port 3 (with an eigenfrequency f_1) is working, the cavity at port 4 (with an eigenfrequency f_2) is at a detuned status and functions as a shorting plane. Therefore, the expanded polarizer degenerates into the normal one. The situation is the same when the cavity at port 4 is working. In the case of a CC, the bandwidth of a resonant cavity (several hundreds of kHz) is much smaller than the frequency interval (several MHz) of adjacent modes. As a result, although two cavities are attached to one expanded polarizer, each of them occupies the polarizer independently at its own frequency span. This provides a very effective method to reduce the polarizers' number in a CC to achieve a lower transmission loss and a more compact size. It should be noted that the length of the circular waveguide on the resonant cavity must be determined during simulation to satisfy the shorting condition at the port of the polarizer.

III. DESIGN OF THE PULSE COMPRESSION SYSTEM

The two-stage rf pulse compression system consists of the CC, SC1, and SC2, as shown in Fig. 1. The SC2 can be detuned to switch the system to the one-stage pulse compressor to generate flattop output. In this section, we use a time-domain method to calculate the output waveform of the pulse compressor system and optimize the system as a two-variables problem. The rf design of each component is also introduced in detail.

A. Parameter design of the rf pulse compression system

The output waveform for a cavity-based rf pulse compression system can be calculated by Fourier transformation [25]. Alternatively, we can calculate the output signals by successively solving the time-domain equation of a detuned SLED numerically, which is described in Appendix A. Because the time-domain equation only involves the complex envelope information of the signal, its calculation is faster than the frequency-domain one, which can save time in the parameter design process.

The performance of the rf pulse compression system is dependent on the frequency (f), unloaded quality factor (Q_0), and coupling factor (β) of working modes in all cavities [25]. In this design, we adopted the spherical cavity design in Refs. [14,25] and determined the Q_0 of each mode. Specifically, correction cavities work in the TE_{112} mode with an unloaded quality factor of $Q_c \approx 4.5 \times 10^4$, and storage cavities work in the TE_{114} mode with an unloaded quality factor of $Q_s \approx 9.2 \times 10^4$. The number of cavities in the CC was set to 8, considering the total size of the system and the amplitude of ripples of the one-stage output [25]. The frequencies of SC1 and SC2 were determined by the power source, 11.424 GHz. Frequencies of the CC were determined

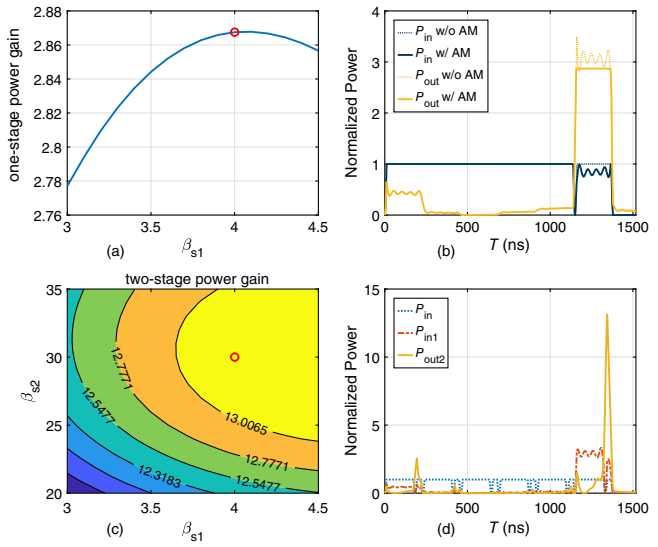

FIG. 4. Calculated power gains with different coupling factors and waveforms of one-stage and two-stage pulse compression. (a) Power gain of one-stage pulse compression versus coupling factor of the first storage cavity. (b) Input and output waveforms of the one-stage pulse compression with $\beta_{s1} = 4.0$ in the case with and without amplitude modification. (c) Power gain of the two-stage pulse compression versus coupling factor of the first and second storage cavities. (d) Input and output waveforms of the two-stage pulse compression with $\beta_{s1} = 4.0$, $\beta_{s2} = 30$. Red circles in (a) and (c) indicate the optimized coupling factor.

by the one-stage output pulse width, which is set to 230 ns. Therefore, the frequency interval of the CC spectrum is $\Delta f = 1/\Delta t = 4.4$ MHz.

A compression ratio (C_r) of 6 was used in the first-stage pulse compression because the flat part of the klystron output is approximately 1.5 μs. A C_r of 5 is used for the second-stage compression. The β of each cavity was free to be optimized. According to Ref. [30], the one-stage pulse compression system generates an approximate flattop output when the external quality factor of the CC is close to that of the SC1. As a result, only β of the SC1 and SC2 were left to be optimized to get a higher power gain, which simplified the optimization process to a two-variables problem.

Power gains as a function of coupling factors are shown in Figs. 4(a) and 4(c) for the one-stage and two-stage pulse compression, respectively. A 10% transmission loss was taken into account during the calculation, corresponding to four dual-mode polarizers in the system. The amplitude modulation (AM) was applied to the input signal to eliminate ripples in the one-stage pulse compression. The β of the SC1 and SC2 were selected as $\beta_{s1} = 4.0$, $\beta_{s2} = 30$, as shown in the red circle in Fig. 4. The calculated waveforms of one-stage and two-stage pulse compression after optimization are shown in Figs. 4(b) and 4(d). The flattop power gain of the one-stage compression and peak power gain of the two-stage compression are 2.87 and 13.2, respectively.

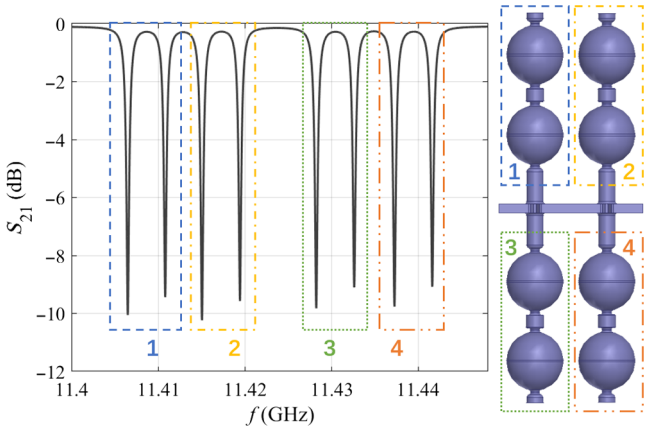

FIG. 5. Vacuum model and simulated transmission spectrum of CC. The dotted boxes show the correspondence between cavity pairs and resonant peaks.

B. rf design of the pulse compression system

The CC adopted the coupled two-cell scheme as the resonant cavity, which can reduce the number of polarizers by half [25]. The polarizer of it adopted the expanded design. Only two polarizers are needed in this eight-cavity CC, as shown in Fig. 5. The CC consists of four units. The two cells of each unit were coupled via a small cylindrical cell instead of a coupling hole. This converts the unit to a three-cell system and allows tuning the frequency interval of the two working modes after fabrication. However, the existence of the cylindrical cell also results in a 17% difference in Q_0 of the two modes [25]. The field intensity in the middle cell should be decreased when working in the zero mode to reduce the difference in Q_0. According to the properties of a coupled three-cell system described in Appendix B, this can be accomplished by enlarging the coupling factor between the spherical cavity and cylindrical cell. The radius of the cylindrical cell is decreased to maintain the frequency interval of the two modes. After optimization, the difference in Q_0 of the two modes was reduced to 12%. This value was not further lowered due to dimension restrictions and tuning considerations.

Simulated results for the working modes in all CCs are listed in Table II. The vacuum model and its transmission

TABLE II. Q-factor and coupling factor of each mode in correction cavities.

f (MHz)	Q_0	Q_e	β
11406.4	4.39×10^4	2.31×10^4	1.90
11410.8	4.88×10^4	2.41×10^4	2.02
11415.2	4.39×10^4	2.34×10^4	1.88
11419.6	4.88×10^4	2.44×10^4	2.00
11428.4	4.41×10^4	2.22×10^4	1.98
11432.8	4.87×10^4	2.31×10^4	2.11
11437.2	4.43×10^4	2.20×10^4	2.01
11441.6	4.87×10^4	2.29×10^4	2.11

TABLE III. Parameters of storage cavities.

	SC1	SC2
f	11.424 GHz	11.424 GHz
Q_0	9.37×10^4	9.26×10^4
Q_e	2.34×10^4	3.09×10^3
β	4.0	30
E_{peak}@1-W input	8.0 kV/m	7.5 kV/m
H_{peak}@1-W input	45 A/m	23 A/m
S_c@1-W input	172 kW/m^2	38 kW/m^2

spectrum are shown in Fig. 5. The boxes in the figure show the corresponding relation between cavity pairs and resonant peaks.

Storage cavities work in TE_{114} mode, with radii of 58.3 mm, and dual-mode polarizers of them adopted the shape without the bottom cylindrical waveguide [17]. Parameters of the SC1 and SC2 are listed in Table III while their surface field distributions are shown in Fig. 6. The maximum surface electric field E_{peak} and modified Poynting vector S_c [31] of SC1 are located at the coupling hole while the maximum surface magnetic field H_{peak} is located at the equator of the spherical cavity. Unlike SC1, the peak surface field of SC2 is located at the dual-mode polarizer because most of the input power is reflected by the cavity owing to its large coupling factor.

To switch the pulse compression system from the two-stage compression mode to the one-stage mode during operation, we designed a detuning rod to detune SC2, similar to the one introduced in Ref. [32]. Simulation shows that a stainless-steel rod with a diameter of 4 mm and length of 60 mm stretched from the top of the spherical cavity can detune it with 30 MHz, which is sufficient for operation.

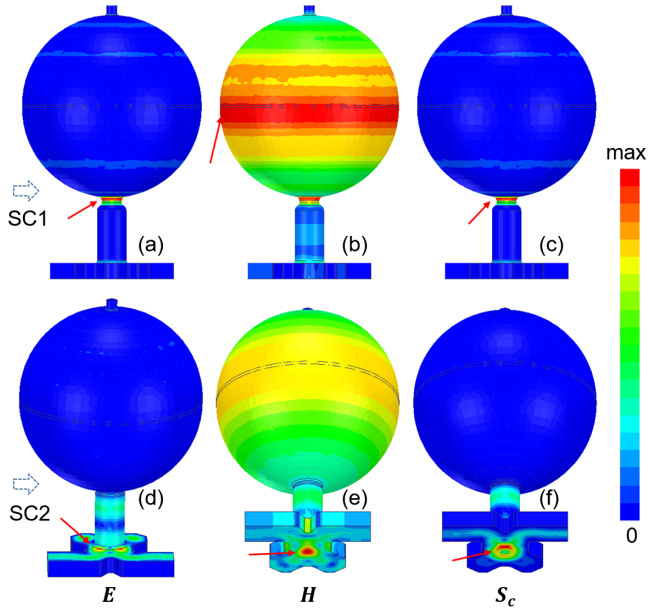

FIG. 6. Surface field of storage cavities. (a)–(c) are surface electric field, magnetic field, and modified Poynting vector of SC1. (d)–(f) are surface electric field, magnetic field, and modified Poynting vector of SC2. Arrows point to maximum locations.

IV. FABRICATION, TUNING, AND RF MEASUREMENT

Mechanical designs of the CC and storage cavities are shown in Fig. 7. The flange-to-flange distance of the CC is

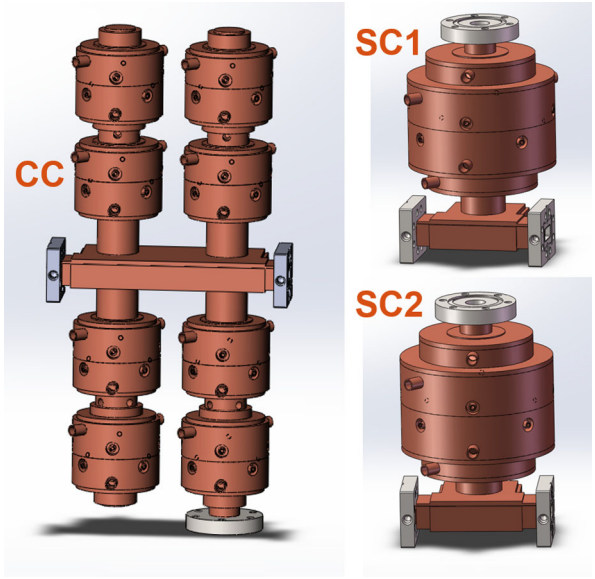

FIG. 7. Mechanical design of the correction cavity chain and storage cavities.

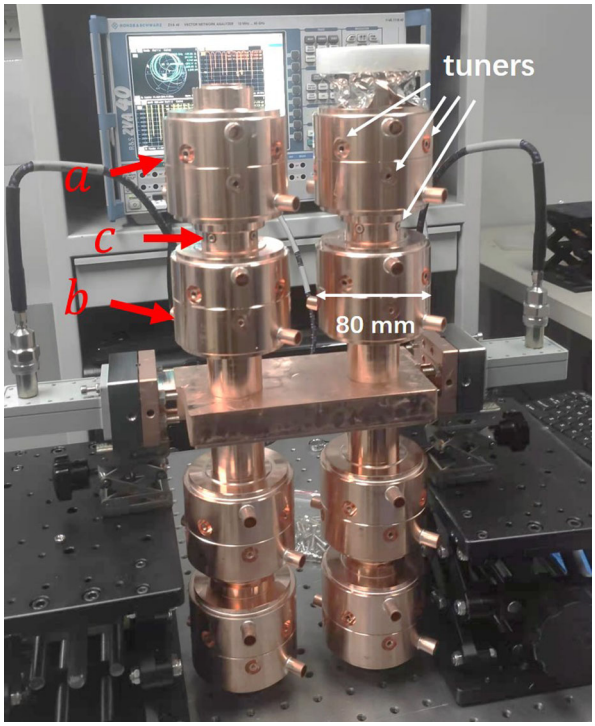

FIG. 8. Microwave measurement of the correction cavity chain during tuning.

TABLE IV. Tuning strategy of a unit in the correction cavity chain.

Priority	Mechanical errors[a]	Judgment	Criteria
1	$\bigcirc a, \bigcirc b$	S_{11}	S_{11} as small as possible
2	$\oslash a \neq \oslash b$	S_{21}	$\beta_{m,1} \approx \beta_{m,2}$[c]
3	$\oslash c$	$\lvert f_{m,1} - f_{m,2}\rvert$[b]	$\lvert f_{m,1} - f_{m,2}\rvert = \lvert f_1 - f_2\rvert$[d]
4	$\oslash a, \oslash b$	$f_{m,1}, f_{m,2}$	$f_{m,1} = f_1, f_{m,2} = f_2$

[a]$\bigcirc$:roundness, $\oslash$:diameter, a, b, and c are the three cells of a unit, as shown in Fig. 8.
[b]$f_{m,1}, f_{m,2}$ are local minimum points in S_{21} curve.
[c]$\beta_{m,1}, \beta_{m,2}$ are measured coupling factor from S_{21} at $f_{m,1}, f_{m,2}$.
[d]f_1, f_2 is the designed resonant frequencies of the unit.

only 230 mm. Two storage cavities adopted a similar design, with a flange-to-flange distance of 130 mm. CF 35 flanges were equipped in the CC and each storage cavity for pumping or application of detuning device.

The CC was measured and tuned after brazing, as shown in Fig. 8. Three coupled cavities were regarded as a tuning unit, and four units can be tuned independently. The tuning process was guided and monitored by the measured S-parameters. To simplify the tuning process, we proposed a tuning strategy based on priority, as shown in Table IV. Tuning should follow this priority order because accomplishing tasks with higher priorities ensures the validity of criteria at the lower priority. For example, when there exist roundness errors of a cavity (priority 1), the reflection will be significant, and the transmission curve in the polar plot will be distorted from the circle shape (see Appendix C). This will cause difficulty in the measurement of coupling factor (priority 2) and resonant frequencies (priority 3) from S_{21}. In task 4, tuning was uniformly applied to each tuner of cavities a and b in a unit to ensure the criteria of tasks 1 and 2.

S-parameters before and after tuning are shown in Fig. 9. After tuning, the resonant frequencies of each working mode were corrected to the designed values, and the

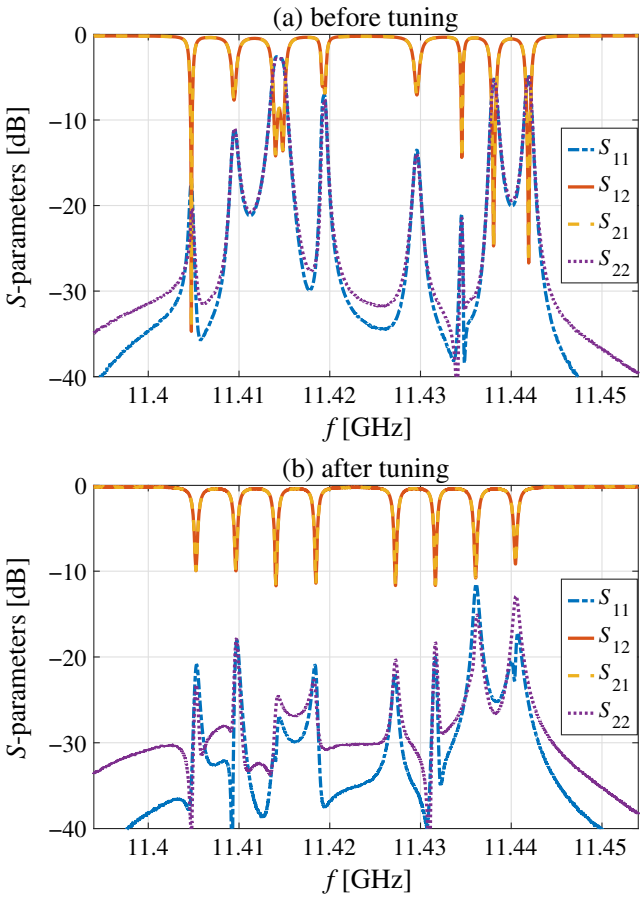

FIG. 9. S-parameters of the correction cavity chain (a) before and (b) after tuning. The transmission loss after tuning is −0.24 dB.

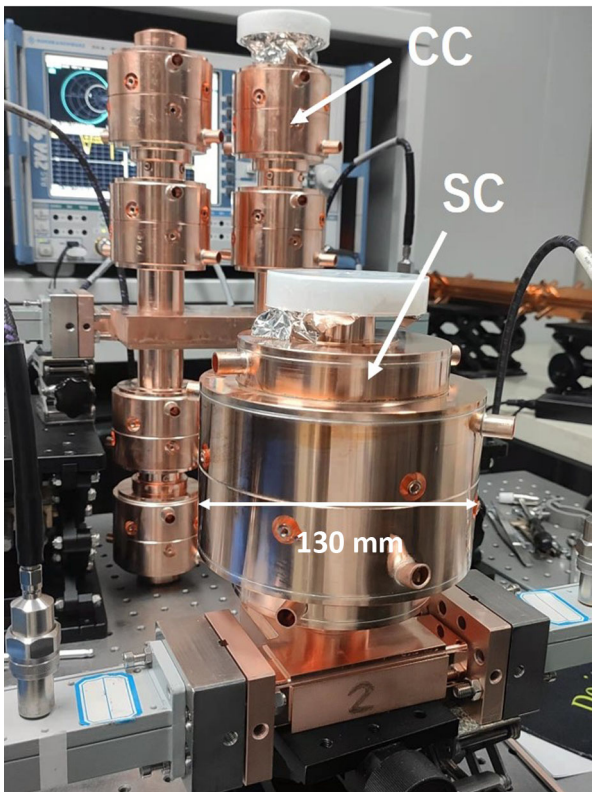

FIG. 10. Microwave measurement of the storage cavity during tuning with the correction cavity chain measured simultaneously.

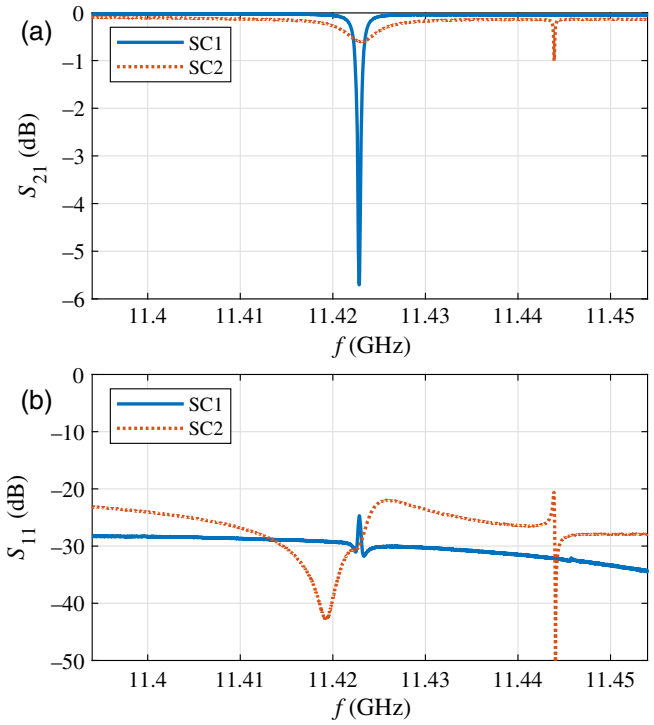

FIG. 11. Transmission (a) and reflection spectrum (b) of the storage cavities after tuning.

reflection was much smaller. Compared with the one in Ref. [25], the transmission loss is about half, achieved by the expanded polarizer. The unloaded quality factor and coupling factor of each mode measured from the S_{21} parameter vary from 4.2 to 4.8×10^4 and 1.7 to 2.0, respectively, which are very close to the designed values.

Tuning of the storage cavities is more straightforward than the CC component. Parameters of each polarized mode of the storage cavities can be derived from the S-parameters with Eq. (C7) in Appendix C. Nonetheless, a more direct tuning strategy was utilized, similar to that in Table IV, but only involves tasks 1 and 4 for a single cavity. To eliminate the environmental influence, we measured the CC simultaneously when tuning the storage cavity to confirm the relative frequency, as shown in Fig. 10.

S-parameters after tuning are shown in Fig. 11. In the transmission spectrum of SC2, there is a tiny resonant peak at 11.443 GHz, which is the TE_{014} mode. Reflections of the SC1 and SC2 at 11.424 GHz are less than −25 dB. Q_0 of the SC1 and SC2 measured from the S_{21} spectrum are 8.8×10^4 and 8.2×10^4, while β are 3.2 and 28, respectively. The β of SC1 is 20% less than the designed value because of poor machining precision, which causes a 4% and 8% degradation in power gain of the one-stage and two-stage output, respectively.

V. HIGH-POWER TEST

The two-stage rf pulse compression system was high-power tested at the Tsinghua X-band high-power test stand (TPOT-X) [33], powered by a 50-MW klystron with a maximum repetition rate of 40 Hz. A schematic diagram of TPOT-X after installing the rf pulse compression system is shown in Fig. 12. TPOT-X is divided into a power source room and a shielded room. The klystron, high-voltage modulator, and low-level rf system are placed in the power source room, while the rf structures under test are installed in the shielded room. The low-level rf system includes a

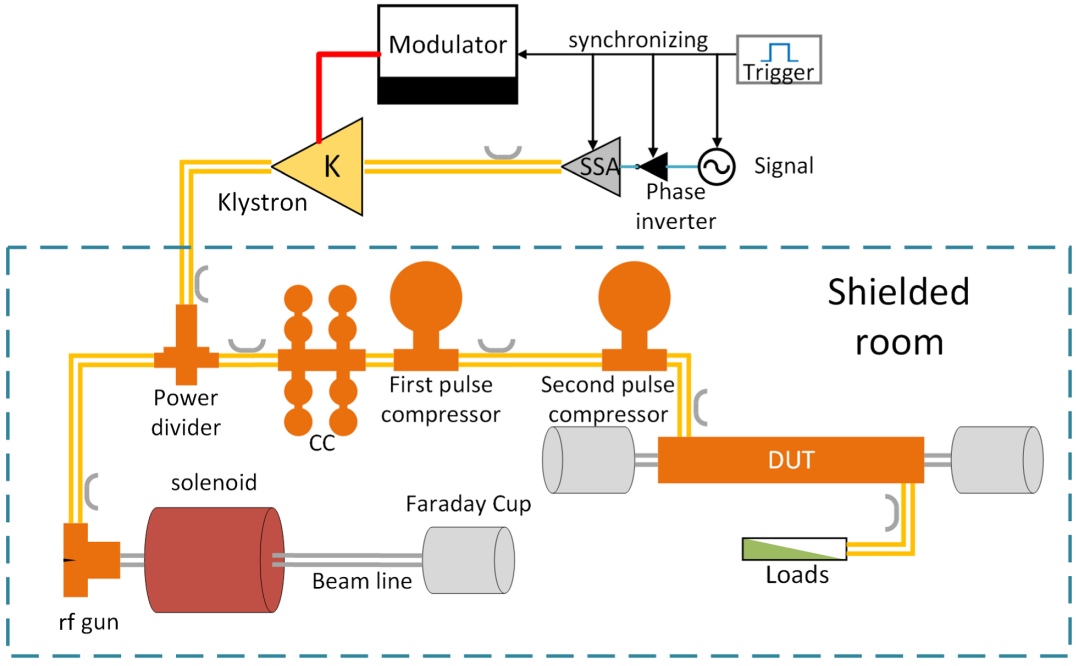

FIG. 12. System diagram of Tsinghua high-power test stand (TPOT-X) with the two-stage pulse compression system installed.

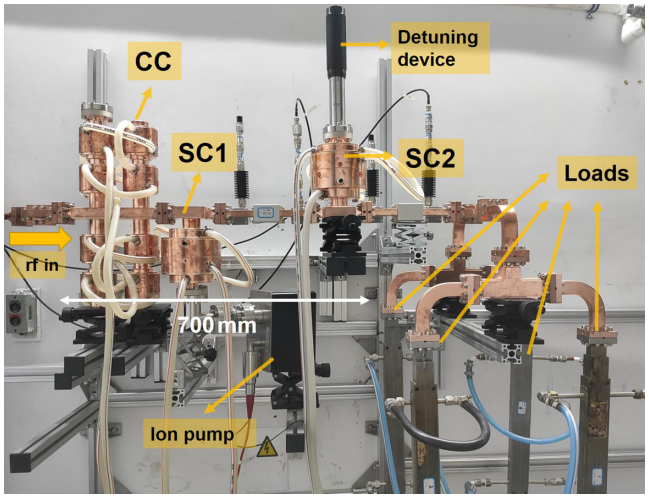

FIG. 13. Photograph of the pulse compression system with four stainless steel loads after installation.

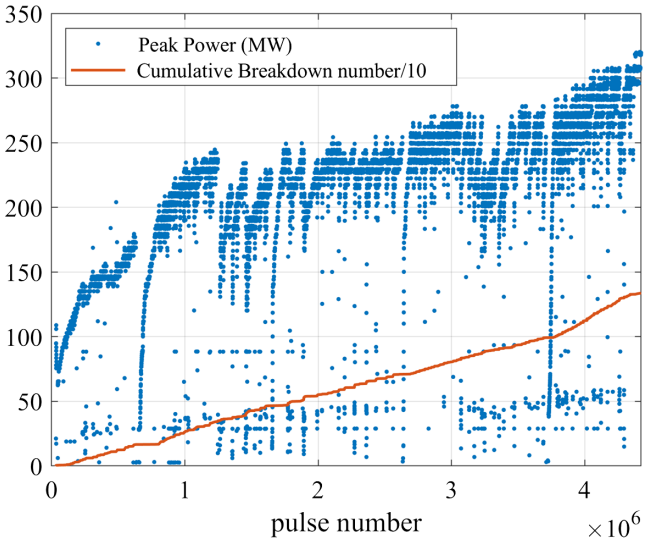

FIG. 14. Condition history of the two-stage pulse compression system at TPOT-X.

signal generator, phase inverter, and solid-state amplifier (SSA), as shown in Fig. 12. The phase inverter can perform multiple phase reversals as well as AM to the signal from the generator for the pulse compression experiment. An adjustable power divider [34] was installed at the platform and split the microwave into a standing-wave branch and a traveling-wave one. The two-stage pulse compression system was tested at the traveling-wave branch in this experiment.

The two-stage pulse compression experiment was expected to output a peak power larger than 300 MW. Therefore, four X-band stainless-steel rf loads scaled from the S-band one [35] were installed at the exit of the pulse compression system to ensure absorption of the output microwave, as shown in Fig. 13. Directional couplers were placed in front of the CC, behind the SC1 and SC2, to extract the corresponding signals. An oscilloscope measured extracted signals from the directional couplers with coaxial attenuators and crystal detectors.

The pulse compression system was first conditioned in the two-stage mode. The system reached a power level of 320 MW after conditioning with 4.5×10^6 pulses at a repetition rate of 40 Hz. The conditioning ceased because power from the klystron was reaching its limit. The conditioning history is shown in Fig. 14. After conditioning, the pulse compression system was operated with an output power of 260 MW for 3 h without a breakdown (breakdown rate $<2.3 \times 10^{-6}$/pulse), verifying the feasibility of the system to handle this power level.

Waveforms of the two-stage pulse compression during the high-power test are shown in Fig. 15(a), and the calculated output waveforms (using the measured input waveform and transmission spectrum) are shown in Fig. 15(b). In this experiment, the flattop part of the output pulse from the klystron is approximately 1.2 μs, which is less than 1.5 μs measured before designing the system. Therefore, a C_r of 5 instead of 6 was selected for the first-stage pulse compression with a total input pulse width of 1150 ns. The C_r of the second-stage pulse compression was 5 as designed. The peak value of the output waveform in Fig. 15(a) is 260 MW, with an average input power of 26.8 MW. Therefore, the peak power gain is 9.7, which has exceeded the theoretical limit of a single-stage pulse compression of 9. The measured power gain was less than

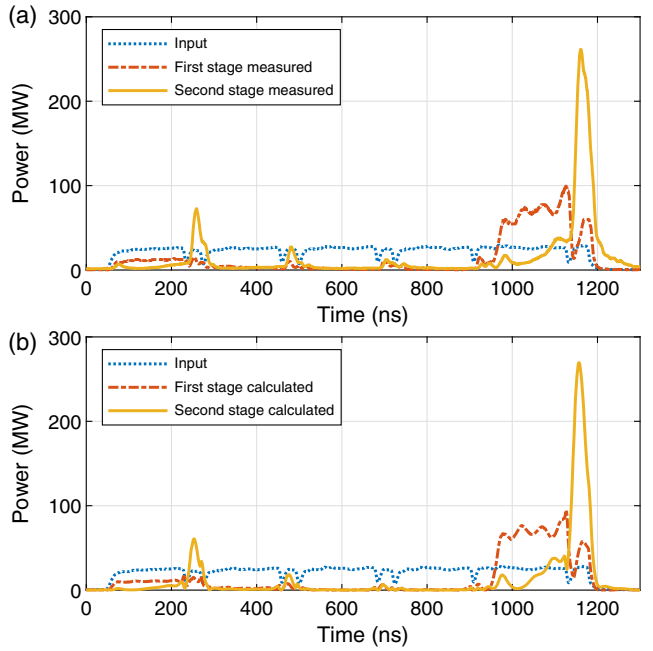

FIG. 15. Waveforms of the two-stage pulse compression high-power test. (a) Measured waveforms of the input, first-stage output, and second-stage output. (b) Measured waveforms of the input and calculated waveforms of the first- and second-stage output.

TABLE V. Peak surface parameters of storage cavities during the high-power test.

	SC1	SC2
E_{peak}	23.9 MV/m	107.5 MV/m
H_{peak}	134 kA/m	303 kA/m
S_c	1.5 MW/mm^2	6.6 MW/mm^2
Pulse heating	11 K	17 K

the designed value of 13.2, mainly due to the reduction in C_r and β of SC1. The pulse width, defined as full width at half maximum (FWHM) of the voltage (or square root of power), was 53 ns. The pulse compression efficiency of the two-stage pulse compression system is 34.3%.

Peak surface parameters of storage cavities were also analyzed when reaching the highest output power, 320 MW. Peak surface fields of SC1 were located inside the cavity. Therefore, they are proportional to the square root of stored energy, which can be calculated from input and output pulse [17]. Peak surface fields of SC2 were located on the polarizer. The surface fields of the polarizer were simulated by setting the driving power at one of the rectangular ports as input power and the driving power at the circular port as output power. Values of input power and output power were obtained from the experiment. Peak surface parameters are shown in Table V, and their locations can refer to Fig. 6. The temperature rise at the maximum point of the magnetic field (pulse heating) was calculated as introduced in Ref. [36]. Comparing with results in high-gradient structures [31,37], S_c in SC2 may be a significant problem in further increasing the output power.

After the two-stage pulse compression test, the SC2 was detuned by stretching the stainless-steel rod into the cavity to convert the system to the one-stage pulse compression. After conditioning with 4.3×10^5 pulses, the system can operate in the one-stage mode with a peak output power of 80 MW, and the flattop power after amplitude modification was 70 MW. After conditioning, the system was tested with a flattop output of 60 MW. Waveforms during the test are shown in Fig. 16(a). The pulse width of the input signal is 1150 ns, with a C_r of 5. The output waveforms after the first-stage and second-stage compression are nearly the same, except for a slight difference in amplitude, which verifies the feasibility of the detuning device. Amplitude modification was applied by the phase inverter to eliminate ripples of the output waveform. Owing to the nonlinearity in the amplification process of the SSA and klystron, the AM function is difficult to calculate in advance. Therefore, we adjust the AM function manually by monitoring the output signal. The output signal after modification is shown in Fig. 16(b). The flattop power gain is 3.0. Because the first ripple before AM is much lower than the others, it has been modified as the rising edge. As a result, the rise time (width from 0.1 to 0.9 maximum) of the output signal after

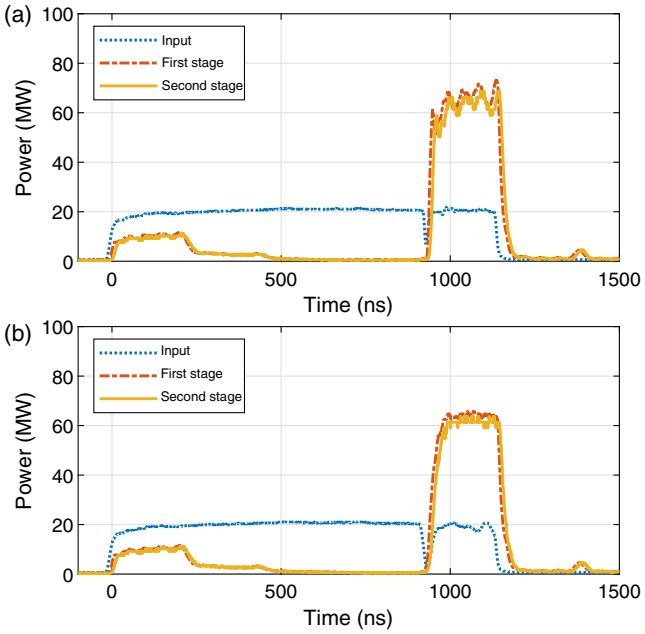

FIG. 16. Waveforms of the pulse compression system (a) with and (b) without amplitude modification when the second-stage storage cavity was detuned.

modification is 35 ns. This also explains that the measured gain factor is higher than the designed value, 2.87. The flattop width (full width at 0.9 maximum) is 181 ns. Inside the flattop part, there is a 150-ns part with a standard deviation of only 1.5% in power amplitude. The falling time (width from 0.9 to 0.1 maximum) of the output pulse is 42 ns, which is caused by the ripples introduced by the CC. The pulse compression efficiency of the one-stage compression is 42.4%.

The one-stage pulse compression experiment shows that the AM effectively eliminates ripples of the output pulse. When applying this system to accelerating structures, the compensation of beam loading requires that the input pulse should have a ramp-up during the filling time [25], which the AM can also accomplish. However, the AM requires that the input signal of the klystron is not saturated, which introduces instability from the klystron. A better scheme is applying phase-to-amplitude modification in a two-klystron unit [19], which has a more stable output than the AM in the single-klystron unit.

Another concern of the output pulse is its phase stability. We used an oscilloscope with a sampling rate of 80 GHz to measure the input and output signal phases. The measured results are shown in Fig. 17. The phases of the input pulse have a standard deviation of 2° after phase reversal, which is likely to be brought by the klystron's response to the phase reversal. After compression, the standard deviation of the phase is less than 1°, in both cases with and without AM. The fluctuation after compression is smaller than the input because the output field is composed of the emitted field and reflected field, while the former comes from the

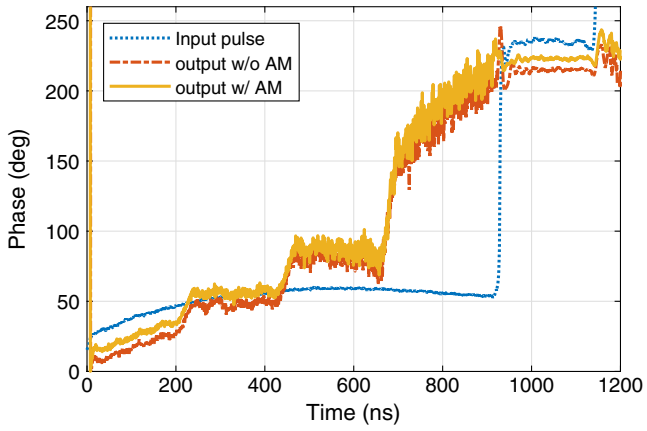

FIG. 17. Phase information of the one-stage pulse compression.

storage cavity and has a stable phase. This high-power test demonstrates that a one-stage pulse compression with a CC can realize stability both in the amplitude and phase which is suitable for the multibunch acceleration in structures.

VI. CONCLUSION

The design and test of a compact X-band two-stage rf pulse compression system were described. Improvement of the correction cavity chain was proposed and verified. The rf pulse compression system can switch between the two-stage and one-stage pulse compression modes. In the two-stage mode, a 53-ns and up to 320-MW pulse is outputted, which can be applied to short-pulse high-gradient structures or high-power microwave devices. In the one-stage mode, a flattop output is realized, demonstrating the correction cavity chain as a high-efficient and compact insertion device to assist the existing pulse compressors in generating flattop outputs.

ACKNOWLEDGMENTS

This work was supported by the National Natural Science Foundation of China (NSFC) No. 11922504.

APPENDIX A: TIME-DOMAIN EQUATION OF A DETUNED SLED

Time-domain equation of the SLED is derived by analyzing the power equivalence of a storage cavity [1]. However, this does not work when the cavity is detuned (the cavity's resonant frequency is not equal to the frequency of the input power). Such a case can be analyzed with the circuit model [38], as shown in Fig. 18.

According to Ref. [38], the voltage of the resonant cavity can be shown to follow the differential equation:

$$\alpha\frac{\mathrm{d}v_g}{\mathrm{d}t}=\frac{\tau}{2}\frac{\mathrm{d}^2v_c}{\mathrm{d}t}+\frac{\mathrm{d}v_c}{\mathrm{d}t}+\frac{\omega_0^2\tau}{2}v_c, \tag{A1}$$

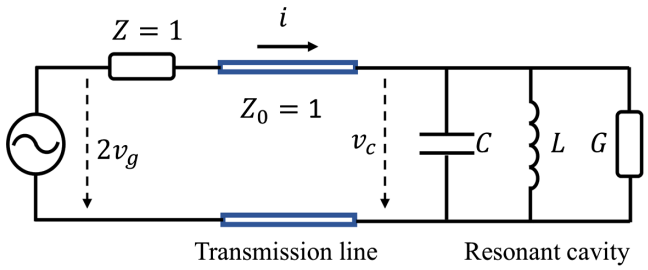

FIG. 18. Equivalent circuit of a storage cavity feed by a generator through a transmission line.

where $\alpha=\frac{2\beta}{1+\beta}$, $\tau=\frac{2Q_0}{\omega_0(1+\beta)}$. v_g and v_c are shown in Fig. 18.

Designating the complex amplitude values with uppercase letters

$$\begin{aligned} v_g&=\Re\{V_g e^{j\omega t}\},\\ v_c&=\Re\{V_c e^{j\omega t}\}. \end{aligned} \tag{A2}$$

Unlike Ref. [38], ω instead of ω_0 is used as the generator's frequency to express a more general case. Insert Eq. (A2) into Eq. (A1), we can get

$$\begin{aligned} \alpha\left(\frac{1}{j\omega}\frac{\mathrm{d}V_g}{\mathrm{d}t}+V_g\right)&=\frac{\tau}{2}\left(\frac{1}{j\omega}\frac{\mathrm{d}^2V_c}{\mathrm{d}t}+2\frac{\mathrm{d}V_c}{\mathrm{d}t}+j\omega V_c\right)\\ &\quad+\left(\frac{1}{j\omega}\frac{\mathrm{d}V_c}{\mathrm{d}t}+V_c\right)+\frac{\omega_0^2\tau}{j2\omega}V_c. \end{aligned} \tag{A3}$$

According to Ref. [38], for a high Q-values cavity and a smoothly varied V_g, all terms in Eq. (A3) with ω in the denominator, except for the last term, can be neglected. This leads to

$$\alpha V_g=\tau\frac{\mathrm{d}V_c}{\mathrm{d}t}+V_c\left(1+\frac{\tau}{2}\frac{\omega_0^2-\omega^2}{j\omega}\right), \tag{A4}$$

which could be further simplified as

$$\tilde{\alpha}V_g=\tilde{\tau}\frac{\mathrm{d}V_c}{\mathrm{d}t}+V_c, \tag{A5}$$

where

$$\begin{aligned} \tilde{\alpha}&=\frac{\alpha}{1+\frac{\tau}{2}\frac{\omega_0^2-\omega^2}{j\omega}}=\frac{2\beta}{1+\beta+jQ_0\xi},\\ \tilde{\tau}&=\frac{\tau}{1+\frac{\tau}{2}\frac{\omega_0^2-\omega^2}{j\omega}}=\frac{2Q_0}{\omega_0(1+\beta+jQ_0\xi)},\\ \xi&=\frac{\omega}{\omega_0}-\frac{\omega_0}{\omega}. \end{aligned} \tag{A6}$$

The time-domain equation of a SLED can still adopt the form in Ref. [38], while an imaginary term $jQ_0\xi$ related to frequency detuning amount is added to α and τ. Furthermore, Eq. (A5) is equivalent to

$$\tilde{\tau}_c \frac{\mathrm{d}E_e}{\mathrm{d}t} + E_e = \tilde{\alpha} E_i. \tag{A7}$$

where E_e is the emitted signal from the cavity, and E_i is the input signal. They are proportional to V_c and V_i, respectively. The output signal of the SLED is given by [1],

$$E_{\mathrm{out}} = E_e - E_i. \tag{A8}$$

Therefore, the response of a detuned SLED can be calculated by solving Eq. (A7) numerically with a given input signal.

APPENDIX B: PROPERTIES OF A SYMMETRIC COUPLED THREE-CELL SYSTEM

According to the coupled resonator model [39], the equivalent circuits equation of a symmetric coupled three-cell system is

$$\begin{bmatrix} 1-\frac{\omega_1^2}{\omega^2} & -\frac{k}{2} & \\ -\frac{k}{2} & 1-\frac{\omega_2^2}{\omega^2} & -\frac{k}{2} \\ & -\frac{k}{2} & 1-\frac{\omega_1^2}{\omega^2} \end{bmatrix} \begin{bmatrix} X_1 \\ X_2 \\ X_3 \end{bmatrix} = \mathbf{0}, \tag{B1}$$

where ω_1 is the resonant frequency of cavities 1 and 3, ω_2 is the resonant frequency of cavity 2, k is the coupling coefficient between cavities 1 and 2 (or 2 and 3), and X_i represents the field in the cavity. The coupling between cavities 1 and 3 is neglected. This equation has a solution if and only if the determinant of the matrix is zero, which leads to

$$a(ab - k^2/2) = 0, \tag{B2}$$

where $a = 1 - \omega_1^2/\omega^2, b = 1 - \omega_2^2/\omega^2$. In Eq. (B2), $a = 0$ give the solution of $\pi/2$ mode:

$$\omega_{\pi/2} = \omega_1, \qquad [X_1 X_2 X_3]^\top = [1, 0, -1]^\top. \tag{B3}$$

By solving $(ab - k^2/2) = 0$, the solution of 0 mode and π mode can be obtained further. For the coupled three-cell system in this article, it satisfies $|\omega_1 - \omega_0| \ll |\omega_2 - \omega_1|$, where ω_0 is the frequency of zero mode. Therefore, the solution of zero mode can be approximated and simplified as

$$\omega_0 \approx \omega_1(1 - k_1), \qquad k_1 = \frac{k^2/4}{\omega_2^2/\omega_1^2 - 1},$$
$$[X_1 X_2 X_3]^\top = [1, 2(1 - \omega_1^2/\omega_0^2)/k, 1]^\top. \tag{B4}$$

Zero mode and $\pi/2$ mode were used in a coupled three-cell unit in the CC. The Q_0 of the zero mode is smaller than $\pi/2$ mode, because the field in cavity 2 is not zero ($X_2 \neq 0$), which results in more surface loss. According to Eq. (B4), the amplitude of X_2 can be reduced by increasing k to improve the Q_0 of zero mode. To maintain the frequency interval (make k_1 unchanged), ω_2 should be increased.

APPENDIX C: S-PARAMETERS OF A POLARIZER WITH AN ELLIPTICAL CAVITY

Because of the machining error in practice, a circular symmetric cavity after fabrication can be regarded as an elliptical one. An essential commission of tuning the compact rf pulse compressor is to compensate for the roundness of the cavity. Therefore, the S-parameters of a dual-mode polarizer with an elliptical cavity need to be studied to evaluate the resonant cavity after fabrication and guide the tuning process.

The scheme of a pulse compressor with an elliptical cavity is shown in Fig. 19. Directions of two polarized modes of the cylindrical waveguide are also shown.

First, the rotation transformation of an orthogonally stimulated device needs to be figured out. The elliptical cavity with a cylindrical waveguide working at the polarized degenerate mode is a two-port device in the microwave network scope, as shown in Fig. 20. When choosing a_1 and a_2 as the input wave, the output wave can be expressed as $\mathbf{b} = \mathbf{Sa}$, where $\mathbf{b} = (b_1, b_2)^\top$, $\mathbf{a} = (a_1, a_2)^\top$. $\mathbf{S}$ is a 2×2 scattering matrix, which depends on the choice of input

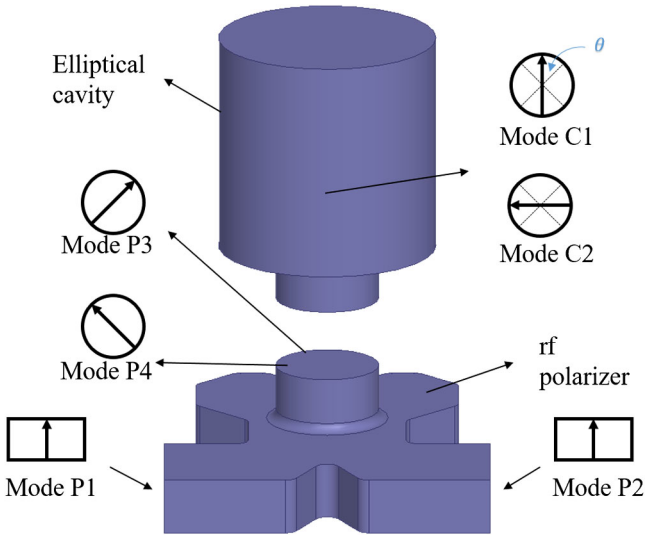

FIG. 19. Scheme of the pulse compressor with an elliptical cavity. Mode Pi denotes the port modes of the waveguide, and mode Ci denotes the polarized eigenmodes of the cavity.

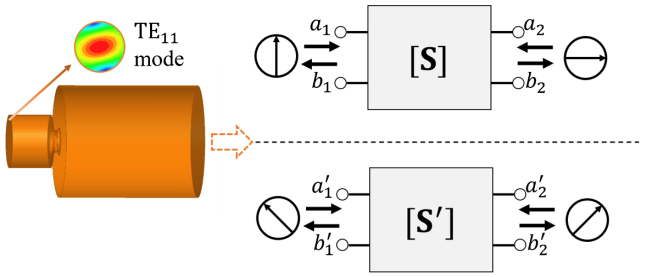

FIG. 20. Schematic diagram of a cavity with a cylinder waveguide working at the polarized degenerate mode.

waves. When choosing a_1' and a_2' as the input wave, we have $\mathbf{b}' = \mathbf{S}'\mathbf{a}'$, where $\mathbf{a}' = (a_1', a_2')^\top$, $\mathbf{b}' = (b_1', b_2')^\top$. $\mathbf{a}$ is not only a combination of input signals but also a vector to notate a polarized mode at an arbitrary angle with a specific orthogonal basis. When $\mathbf{a}$ and $\mathbf{a}'$ are used to notate the same vector, their relationship can be expressed with a rotation matrix $\mathbf{R}_\theta$:

$$\mathbf{a}' = \mathbf{R}_\theta \mathbf{a}, \qquad \mathbf{R}_\theta = \begin{pmatrix} \cos\theta & \sin\theta \\ -\sin\theta & \cos\theta \end{pmatrix}. \tag{C1}$$

Or equivalently, $\mathbf{a} = \mathbf{R}_{-\theta}\mathbf{a}'$, where $\mathbf{R}_{-\theta}$ is a rotation matrix with angle $-\theta$. This conversion can also be applied to $\mathbf{b}$ and $\mathbf{b}'$. Therefore,

$$\mathbf{b} = \mathrm{Sa} \Rightarrow \mathbf{R}_{-\theta}\mathbf{b}' = \mathbf{S}\mathbf{R}_{-\theta}\mathbf{a} \Rightarrow \mathbf{b}' = \mathbf{R}_\theta \mathbf{S}\mathbf{R}_{-\theta}\mathbf{a}. \tag{C2}$$

As a result, the relationship between $\mathbf{S}$ and $\mathbf{S}'$ is

$$\mathbf{S}' = \mathbf{R}_\theta \mathbf{S}\mathbf{R}_{-\theta}. \tag{C3}$$

Second, the scattering matrix of the polarizer as an ideal 3-dB coupler can be expressed as [30]:

$$\mathbf{M}_{3\ \mathrm{dB}} = \begin{bmatrix} \mathbf{0} & \mathbf{T}_{3\ \mathrm{dB}} \\ \mathbf{T}_{3\ \mathrm{dB}} & \mathbf{0} \end{bmatrix}, \quad \mathbf{T}_{3\ \mathrm{dB}} = \frac{1}{\sqrt{2}}\begin{bmatrix} 1 & j \\ j & 1 \end{bmatrix}. \tag{C4}$$

Assuming the reflection spectra of mode C1 and C2 in the elliptical cavity are Γ_1 and Γ_2, respectively, S-parameters of the whole pulse compressor can be calculated with Eq. (3). When the direction of mode C1 and P3 coincide, the relationship matrix in Eq. (3) is $\mathbf{T} = \mathrm{diag}\{\Gamma_1, \Gamma_2\}$. Therefore, S-parameters after cascading is

$$\mathbf{T}_{3\ \mathrm{dB}}\mathbf{T}\mathbf{T}_{3\ \mathrm{dB}} = \frac{1}{2}\begin{bmatrix} \Gamma_1 - \Gamma_2 & j(\Gamma_1 + \Gamma_2) \\ j(\Gamma_1 + \Gamma_2) & \Gamma_2 - \Gamma_1 \end{bmatrix}. \tag{C5}$$

As shown in Eq. (C5), a difference between Γ_1 and Γ_2 will cause a non-negligible reflection in the rectangular ports and distortion of the transmission spectrum. If we rotate the cavity so that directions of mode C1 and P3 have an angle

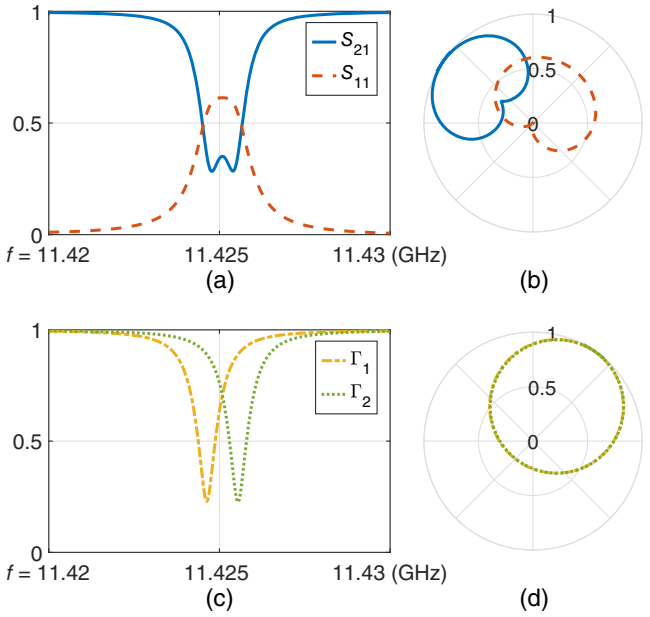

FIG. 21. Simulation of a pulse compressor with an elliptical cavity and reconstruction of reflection spectrum for each polarized mode. (a) Simulated transmission and reflection spectra of a pulse compressor with the elliptical cavity. (b) Polar plot of (a). (c) Reconstructed reflection spectra of two eigenmodes in the elliptical cavity. (d) Polar plot of (c).

of θ, the relation matrix $\mathbf{T}$ goes through a rotation transformation before being cascaded. The scattering matrix after cascaded in this situation is

$$\begin{aligned} &\mathbf{T}_{3\ \mathrm{dB}}(\mathbf{R}_\theta \mathbf{T}\mathbf{R}_{-\theta})\mathbf{T}_{3\ \mathrm{dB}} \\ &= \frac{1}{2}\begin{bmatrix} (\Gamma_1 - \Gamma_2)e^{-j2\theta} & j(\Gamma_1 + \Gamma_2) \\ j(\Gamma_1 + \Gamma_2) & (\Gamma_2 - \Gamma_1)e^{j2\theta} \end{bmatrix}, \end{aligned} \tag{C6}$$

where $\mathbf{R}_\theta$ is the rotation transformation matrix. There is only a phase shift in the reflection coefficient compared with Eq. (C5). According to Eq. (C6), Γ_1, Γ_2, and θ can be reconstructed from S-parameters of the whole pulse compressor:

$$\begin{cases} \Gamma_1, \Gamma_2 = S_{12}/j \pm \sqrt{-S_{11}S_{22}}, \\ \theta = \arg\{-S_{22}/S_{11}\}/4 \end{cases} \tag{C7}$$

where Γ_1 and Γ_2 are reflection spectra of two modes in an elliptical cavity, S_{ij} is the elements of the scattering matrix of a pulse compressor, and θ is the angle between the modes of the cavity and the polarizer. We simulated a polarizer with an elliptical cavity and reconstructed the reflection spectrum of each polarized mode using Eq. (C7), as shown in Fig. 21. The resonant frequency, Q_0, and β derived from the reconstructed reflection spectrum are in accordance with the results from the eigenmode solver.

Therefore, the measurement of S-parameters of a pulse compressor after fabrication can provide information of each polarized mode inside the cavity and guide the tuning.

[1] Z. Farkas, H. Hoag, P. B. Wilson, and G. Loew, SLED: A method of doubling SLAC's energy, in *Proceedings of the 9th International Conference on High-Energy Accelerators, Stanford, CA* (A.E.C., Washington, DC, 1974), p. 576.

[2] A. Fiebig, R. Hohbach, P. Marchand, and J. O. Pearce, Design considerations, construction and performance of a SLED type radiofrequency pulse compressor using very high Q cylindrical cavities, Conf. Proc. C **870316**, 1931 (1987), https://inspirehep.net/literature/245977.

[3] R. Akre, V. Bharadwaj, P. Emma, and P. Krejcik, SLAC LINAC RF performance for LCLS, eConf **C000821**, THc11 (2000), https://arxiv.org/abs/physics/0008171.

[4] J. Arthur, P. Anfinrud, P. Audebert, and K. Bane, Linac Coherent Light Source (LCLS) Conceptual Design Report, Report No. SLAC-R-593, 2002.

[5] H. Matsumoto, H. Baba, S. Yamaguchi, and A. Miura, High power test of a SLED system with dual side-wall coupling irises for linear colliders, Nucl. Instrum. Methods Phys. Res., Sect. A **330**, 1 (1993).

[6] I. Abe *et al.*, The KEKB injector linac, Nucl. Instrum. Methods Phys. Res., Sect. A **499**, 167 (2003).

[7] Y. Joo, H.-S. Lee, W. Hwang, Y. Park, K. Oh, and B.-J. Lee, Design study of a new SLED system with a biplanar 3-dB power divider and dual side-wall coupling-irises for the PAL XFEL, J. Korean Phys. Soc. **63**, 1253 (2013).

[8] W. Chao-Peng, F.-W. Cheng, T. De-Chun, Q. gu, and Z. Zhen-Tang, Design and study of a c-band pulse compressor for the SXFEL linac, Nucl. Sci. Tech. **25**, 4 (2014).

[9] W. Fang, Q. Gu, X. Sheng, C. Wang, D. Tong, L. Chen, S. Zhong, J. Tan, G. Lin, Z. Chen, and Z. Zhao, Design, fabrication and first beam tests of the c-band RF acceleration unit at SINAP, Nucl. Instrum. Methods Phys. Res., Sect. A **823**, 91 (2016).

[10] V. Balakin and I. Syrachev, Status of VLEPP RF power multiplier (VPM), in *Proceedings of the 5th European Particle Accelerator Conference, Barcelona, Spain* (IOP, Bristol, 1996), pp. 1173–1175.

[11] J. Hirshfield, S. V. Kuzikov, M. I. Petelin, and V. G. Pavelyev, Whispering gallery pulse compressor, AIP Conf. Proc. **737**, 637 (2004).

[12] J. Wang, S. Tantawi, and C. Xu, New SLED 3 system for multi-mega watt RF compressor, arXiv:1408.4851.

[13] M. Franzi, J. Wang, V. Dolgashev, and S. Tantawi, Compact rf polarizer and its application to pulse compression systems, Phys. Rev. Accel. Beams **19**, 062002 (2016).

[14] J. W. Wang, S. G. Tantawi, C. Xu, M. Franzi, P. Krejcik, G. Bowden, S. Condamoor, Y. Ding, V. Dolgashev, J. Eichner, A. Haase, J. R. Lewandowski, and L. Xiao, Development for a supercompact X-band pulse compression system and its application at SLAC, Phys. Rev. Accel. Beams **20**, 110401 (2017).

[15] Z.-B. Li, W.-C. Fang, Q. Gu, J.-H. Tan, X.-X. Huang, and Z.-T. Zhao, Design, fabrication, and cold-test results of C-band spherical RF pulse compressor prototype, Radiat. Detect. Technol. Methods **3**, 21 (2019).

[16] P. Wang, J. Shi, H. Zha, D. Cao, M. Peng, Z. Liu, C. Cheng, and H. Chen, Development of an s-band spherical pulse compressor, Nucl. Instrum. Methods Phys. Res., Sect. A **901**, 84 (2018).

[17] Y. Jiang, H. Zha, J. Shi, M. Peng, and H. Chen, A compact x-band microwave pulse compressor using a corrugated cylindrical cavity, IEEE Trans. Microwave Theory Tech. **69**, 1586 (2021).

[18] X. Wu and A. Grudiev, Novel open cavity design for rotating mode rf pulse compressors, Phys. Rev. Accel. Beams **24**, 112001 (2021).

[19] H. Hayano, K. Kubo, T. Naito, K. Oide, T. Shintake, and S. Takeda, Beam loading compensation using phase to amplitude modulation method in ATF, *Proceedings of the XIX International Linear Accelerator Conference* (1998), pp. 91–93.

[20] G. Shu, F.-L. Zhao, S.-L. Pei, and O.-Z. Xiao, RF modulation studies on an s band pulse compressor, Chin. Phys. C **40**, 037002 (2016).

[21] P. B. Wilson, Z. Farkas, and R. D. Ruth, SLED II: A new method of RF pulse compression, Stanford Linear Accelerator Center, Menlo Park, CA, Technical Report No. SLAC-PUB-5330, 1990.

[22] C. Nantista, Z. D. Farkas, N. M. Kroll, T. L. Lavine, A. Manegat, R. D. Ruth, S. G. Tantawi, A. E. Vlieks, and P. B. Wilson, High-power RF pulse compression with SLED-II at SLAC, in *Proceedings of International Conference on Particle Accelerators, Washington, DC, 1993* (IEEE, New York, 1993), p. 1196.

[23] S. G. Tantawi, C. D. Nantista, V. A. Dolgashev, C. Pearson, J. Nelson, K. Jobe, J. Chan, K. Fant, J. Frisch, and D. Atkinson, High-power multimode x-band rf pulse compression system for future linear colliders, Phys. Rev. ST Accel. Beams **8**, 042002 (2005).

[24] S. Y. Kazakov, Pulse shape correction for rf pulse compression system, *3rd European Particle Accelerator Conference* (1992), p. 576, https://accelconf.web.cern.ch/e92/PDF/EPAC1992_1247.PDF.

[25] P. Wang, H. Zha, I. Syratchev, J. Shi, and H. Chen, rf design of a pulse compressor with correction cavity chain for klystron-based compact linear collider, Phys. Rev. Accel. Beams **20**, 112001 (2017).

[26] Y. Jiang, H. Zha, P. Wang, J. Shi, H. Chen, W. L. Millar, and I. Syratchev, Demonstration of a cavity-based pulse compression system for pulse shape correction, Phys. Rev. Accel. Beams **22**, 082001 (2019).

[27] Y. Jiang, J. Shi, P. Wang, H. Zha, X. Lin, F. Liu, C. Cheng, and H. Chen, Compact two-stage pulse compression system for producing gigawatt microwave pulses, IEEE Trans. Microwave Theory Tech. **69**, 4533 (2021).

[28] C. Xu, S. Tantawi, and J. Wang, Conceptual design of x band waveguide dual circular polarizer, Phys. Rev. Accel. Beams **19**, 062003 (2016).

[29] A. Grudiev, Design of compact high power RF components at X-band, Report No. CLIC–Note–1067, 2016.

[30] W. Ping, Research on the novel high-power microwave pulse compressors, Ph.D. thesis, Tsinghua University,

2018, https://kns.cnki.net/KCMS/detail/detail.aspx?dbname=CDFDLAST2020&filename=1020723790.nh.

[31] A. Grudiev, S. Calatroni, and W. Wuensch, New local field quantity describing the high gradient limit of accelerating structures, Phys. Rev. ST Accel. Beams **12**, 102001 (2009).

[32] J. Lei, X. He, M. Hou, G. Shu, G.-X. Pei, X.-P. Li, and H. Wang, RF design of an s-band spherical cavity pulse compressor, Radiat. Detect. Technol. Methods **1**, 16 (2017).

[33] M. Peng, J. Shi, H. Zha, X. Lin, Z. Liu, Y. Jiang, J. Gao, L. Zhou, F. Liu, X. Meng, and H. Chen, Development and high-gradient test of a two-half accelerator structure, Nucl. Sci. Tech. **32**, 60 (2021).

[34] F. Liu, J. Shi, H. Zha, and H. Chen, Development of a compact x-band variable-ratio rf power splitter, Nucl. Instrum. Methods Phys. Res., Sect. A **1015**, 165759 (2021).

[35] X. Meng, J. Shi, H. Zha, Q. Gao, Z. Liu, J. Liu, Y. Jiang, P. Wang, H. Chen, and J. Qiu, Development of high-power s-band load, Nucl. Instrum. Methods Phys. Res., Sect. A **927**, 209 (2019).

[36] D. P. Pritzkau and R. H. Siemann, Experimental study of rf pulsed heating on oxygen free electronic copper, Phys. Rev. ST Accel. Beams **5**, 112002 (2002).

[37] X.-C. Lin, H. Zha, J.-R. Shi, Q. Gao, J.-Y. Liu, L.-Y. Zhou, J. Gao, H.-B. Chen, and C.-X. Tang, Fabrication, tuning, and high-gradient testing of an X-band traveling-wave accelerating structure for VIGAS, Nucl. Sci. Tech. **33**, 102 (2022).

[38] A. Fiebig and C. Schieblich, A SLED type pulse compressor with rectangular pulse shape, Report No. CERN/PS 90-13 (RF) (1990).

[39] D. E. Nagle, E. A. Knapp, and B. C. Knapp, Coupled resonator model for standing wave accelerator tanks, Rev. Sci. Instrum. **38**, 1583 (1967).